AGU PUBLICATIONS

JGR

Journal of Geophysical Research: Oceans

RESEARCH ARTICLE

10.1002/2016JC012455

Key Points:
- Intense mixing occurs in highly stratified estuaries as a result of laterally divergent, supercritical flow during ebb
- Mixing zones have nearly continuous shear instability and nearly constant gradient Richardson number close to the critical value of 0.25
- Turbulence intensity, quantified by dissipation of turbulent kinetic energy, can be estimated based on the hydraulic state and flow geometry

Correspondence to:
W. R. Geyer,
rgeyer@whoi.edu

Citation:
Geyer, W. R., D. K. Ralston, and R. C. Holleman (2017), Hydraulics and mixing in a laterally divergent channel of a highly stratified estuary, *J. Geophys. Res. Oceans*, *122*, 4743–4760, doi:10.1002/2016JC012455.

Received 9 OCT 2016
Accepted 5 MAY 2017
Accepted article online 15 MAY 2017
Published online 12 JUN 2017

Hydraulics and mixing in a laterally divergent channel of a highly stratified estuary

W. Rockwell Geyer[1], David K. Ralston[1], and Rusty C. Holleman[2]

[1]Applied Ocean Physics and Engineering, Woods Hole Oceanographic Institution, Woods Hole, Massachusetts, USA, [2]San Francisco Estuary Institute, Richmond, California, USA

Abstract Estuarine mixing is often intensified in regions where topographic forcing leads to hydraulic transitions. Observations in the salt-wedge estuary of the Connecticut River indicate that intense mixing occurs during the ebb tide in regions of supercritical flow that is accelerated by lateral expansion of the channel. The zones of mixing are readily identifiable based on echo-sounding images of large-amplitude shear instabilities. The gradient Richardson number (Ri) averaged across the mixing layer decreases to a value very close to 0.25 during most of the active mixing phase. The along-estuary variation in internal Froude number and interface elevation are roughly consistent with a steady, inviscid, two-layer hydraulic representation, and the fit is improved when a parameterization for interfacial stress is included. The analysis indicates that the mixing results from lateral straining of the shear layer, and that the rapid development of instabilities maintains the overall flow near the mixing threshold value of Ri = 0.25, even with continuous, active mixing. The entrainment coefficient can be estimated from salt conservation within the interfacial layer, based on the finding that the mixing maintains Ri = 0.25. This approach leads to a scaling estimate for the interfacial mixing coefficient based on the lateral spreading rate and the aspect ratio of the flow, yielding estimates of turbulent dissipation within the pycnocline that are consistent with estimates based on turbulence-resolving measurements.

1. Introduction

Many authors have described the role of topographically induced hydraulic transitions in generating estuarine mixing, usually associated with hydraulic jumps from supercritical to subcritical flow [e.g., *Partch and Smith*, 1978; *Farmer and Smith*, 1980; *Farmer and Armi*, 1999]. Indeed the dramatic overturn structures that are often observed in hydraulic jumps, most notably in the acoustic images of *Farmer and Armi* [1999], strongly support the connection between hydraulics and mixing. A few studies have addressed mixing specifically associated with supercritical internal Froude numbers [e.g., *Geyer and Farmer*, 1989; *Chant and Wilson*, 2000; *Peters*, 2003; *MacDonald and Horner-Devine*, 2008], in regions where no jump occurred but the accelerating supercritical flow became unstable to shear instabilities. Most relevant to this study is the analysis by *Chant and Wilson* [2000] of the hydraulics of supercritical flow in an expansion, wherein the conservation of spanwise vorticity leads to an intensification of shear, thus lowering the gradient Richardson number $Ri = -(g/\rho)(\partial\rho/\partial z)/(\partial u/\partial z)^2$, and leading to mixing. Chant and Wilson suggested that this mechanism should lead to enhanced mixing in particular reaches of the Hudson River, and *Peters* [2003] confirmed their hypothesis with turbulence measurements as well as estimates of Ri that indicated lower Ri and enhanced mixing in expansions during supercritical ebb flows.

Similar results have been obtained in the nearfield of river plumes, in which lateral spreading of the supercritical outflow causes a reduction of Ri and enhanced mixing [*MacDonald and Geyer*, 2004; *MacDonald and Chen*, 2012; *Jurisa et al*., 2016]. MacDonald and Geyer parameterize the mixing within the Fraser River plume with an interfacial drag coefficient, but they do not investigate its potential dependence on the geometry of the outflow. *MacDonald and Chen* [2012] also report an interfacial mixing parameter (related to interfacial drag through the mixing efficiency) for the Merrimack River outflow, demonstrating that it increases monotonically with lateral spreading rate. They suggest that lateral spreading amplifies the vorticity within Kelvin-Helmholtz billows in the shear layer, similar to the explanation of *Chant and Wilson* [2000] for the augmentation of mixing due to amplification of shear.

Jurisa et al. [2016] do not address the spreading rate, but they effectively parameterize mixing in the Columbia River plume via an Ri-dependent expression from *Kunze et al*. [1990]. The expression of *Kunze et al*. [1990] is based on theoretical growth rates of shear instabilities [*Hazel*, 1972] as Ri falls below its critical value. In their analysis, Jurisa et al. assumed a critical value of Ri (or Ri_{crit}) of 0.5 rather than the theoretical 0.25. This was justified based on oceanic observations of mixing by *Polzin* [1996], who selected a value $Ri_{crit} = 0.4$. A higher value of Ri_{crit} is not based on theory, which unambiguously defines $Ri_{crit} = 0.25$ [*Miles*, 1961; *Hazel*, 1972]. The selection of a higher threshold could be due to measurement issues, notably underresolving the vertical shear, which would lead to overestimation of Ri. Despite advances in measurement techniques, Ri remains a difficult quantity to quantify due to its dependence on the square of the vertical shear. The temporal and spatial scales of measurement that are required to accurately parameterize mixing remain to be determined [*Balsley et al*., 2008].

This paper seeks to demonstrate that the mixing in a stratified shear layer can be estimated based on the hydraulic response of an expanding, supercritical flow. The details of the gradient Richardson number distribution are not required, but only the assumption that mixing occurs when $Ri < Ri_{crit}$, and that as a result of the mixing, the flow adjusts back to the condition $Ri \approx Ri_{crit}$. This behavior is consistent with the laboratory experiments of *Thorpe* [1973] and numerous observations [e.g., *Geyer and Smith*, 1987; *Peters et al*., 1988], with the caveat that the equilibrium value of Ri may be slightly larger than the theoretical value of 0.25. Using the same rationale as *Trowbridge* [1992], the rate of mixing is determined by the amount of vertical transport of momentum and mass to maintain the $Ri = 0.25$ condition, satisfying the two-layer hydraulic equations with the addition of an interfacial mixing term [e.g., *Schijf and Schonfeld*, 1953]. The results of the analysis suggest that the effective mixing coefficient (or entrainment coefficient as defined by *Ellison and Turner* [1959]) can be estimated based on the geometry of the flow, notably its aspect ratio (width to depth) and lateral expansion rate. The method quantitatively predicts the mixing coefficients reported by *MacDonald and Chen* [2012] as well as by *MacDonald and Geyer* [2004], and may have relevance to the scaling of entrainment rates for oceanic overflows [*Cenedese and Adduce*, 2010].

The field site of the study is the highly stratified Connecticut River estuary, in which high-resolution measurements of the vertical structure of the flow and density structure were combined with turbulence-resolving measurements as well as high-resolution acoustic backscatter measurements to document the occurrence of shear instabilities. This paper specifically addresses the ebb in a reach of the estuary where flow passes through a constriction and a downstream expansion. The flow expansion is dynamically analogous to the near-field conditions of a river outflow [*Hetland*, 2010; *Horner-Devine et al*., 2015], with similar intensification of mixing.

The paper also provides an analysis of the mixing rate based on an isohaline coordinate system, which allows a separation of isohaline and diahaline fluxes, the latter being a combination of entrainment and vertical diffusion. The relationship between entrainment and diffusion derived by *McDougall and Dewar* [1998] is used to provide quantitative estimates of turbulent salt and momentum flux within the pycnocline based on the observed variations of the Reynolds-averaged velocity and salinity. These estimates are compared to previously published estimates of turbulent dissipation and salt flux at the study site using turbulence-resolving sensors [*Holleman et al*., 2016].

The paper is organized as follows. Section 2 provides a brief description of the field measurement program. Section 3 presents the observational results, notably the evidence for intensified mixing in the laterally expanding channel, and the evidence for asymptotic behavior of the gradient Richardson number (i.e., $Ri \approx 0.25$) under strong mixing conditions. Section 4 applies two-layer hydraulic theory in combination with a critical gradient Richardson number constraint to obtain a relationship between the hydraulic forcing by lateral spreading and mixing, and tests the parameterization against turbulence measurements obtained during the same field campaign [*Holleman et al*., 2016]. Section 5 discusses the application of the results to other estuaries, river plumes and oceanic overflows and compares the gradient Richardson number observations to other studies. Section 6 provides a summary. The appendix provides a derivation of the expression for the interfacial drag coefficient based on momentum and volume conservation in a laterally spreading, stratified shear layer.

2. Field Measurements

The Connecticut River estuary is an energetic, tidally forced salt wedge, exhibiting rapid frontal advance during the flooding tide and intense mixing and breakdown of the salinity structure during ebb, similarly to

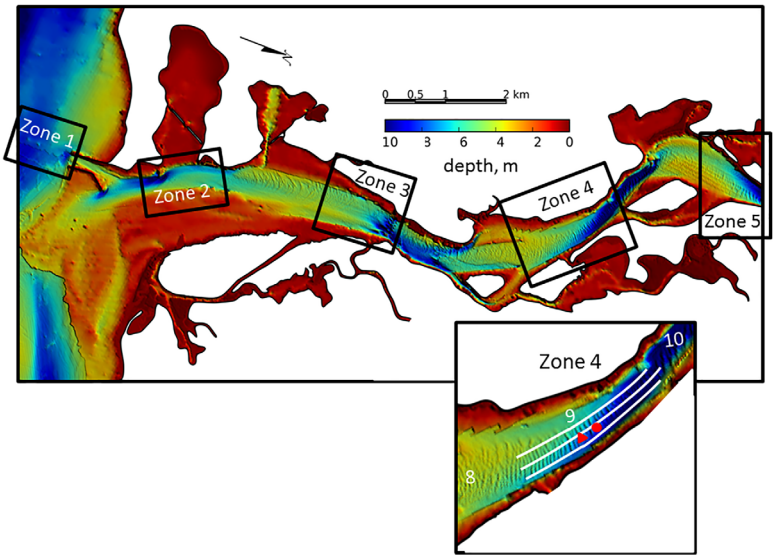

Figure 1. Bathymetric map of the Connecticut River estuary (color contours of depth in m), with the five zones where intensified mixing was observed during ebb in association with lateral expansions. An inset provides more detail of Zone 4, where intensive ebb measurements were performed, including several ship tracks during the 2013 surveys (white lines) and the location of the timeseries mooring from 2015 (red triangle: upward-looking ADCP, red circle: mooring with seven evenly spaced T-S sensors). The high-resolution bathymetry indicates the presence of sand waves throughout the estuary.

the Fraser [*Geyer and Farmer*, 1989] and the Merrimack [*Ralston et al*., 2010] estuaries. Moored and shipboard observations were performed in November 2013 during low to moderate discharge conditions ($Q = 200–450$ m^3/s at USGS gage at Thompsonville, CT, where long-term average $Q \approx 550$ m^3/s), and again in September–October 2015 during predominantly low discharge conditions (100–200 m^3/s with a brief freshet of 1100 m^3/s). Moored measurements during the 2015 measurements included an upward-looking acoustic Doppler current profiler (ADCP) (1.2 MHz frequency) and a vertical array of seven RBR conductivity-temperature sensors, three of which also had pressure sensors to determine the vertical sensor separation. Shipboard measurements included a 1.2 MHz ADCP, a continuously profiling conductivity-temperature-depth (CTD), and a multifrequency array of broadband acoustic transducers to resolve backscatter off the density interface [*Lavery et al*., 2013]. In addition, a vertical array of turbulence-resolving sensors was mounted on a mast deployed from the bow of the research vessel, as described by *Holleman et al*. [2016].

A notable finding of these observations was the intensification of mixing during the ebb in regions of lateral expansions, shown as Zones 1–5 on Figure 1. Earlier investigations by *Geyer et al*. [2010] and *Lavery et al*. [2013] identified intensified mixing by shear instabilities in Zones 1 and 3. The focus here is on data obtained in "Zone 4" (Figure 1), a lateral expansion (with respect to the ebb tide) in the upper portion of the estuary, between 8 and 10 km from the mouth. Three closely spaced along-channel lines were occupied by the vessel during ebb tides on 4 and 5 November 2013, with lines repeated approximately every 20 min. The moored ADCP (red triangle) and vertical T-S array (red circle) were deployed in the same region from 26 September 2015 to 3 November 2015.

3. Results

The velocity and salinity show strong shear and stratification, with similar vertical structure along the region of the expansion during the ebb, as shown in several selected lines close to maximum ebb (Figure 2). The pycnocline tilts upward in the downstream direction, and the slope of the velocity contours was the same as the salinity contours. Earlier in the ebb (top), the pycnocline is closer to the surface, and it moves lower in the water column as the ebb progresses. The velocity reaches as high as 1.6 m/s in the upper layer, and it remains close to zero (or even slightly flooding) near the bottom until the later ebb, when near-bottom velocities are seaward at 0.2–0.4 m/s. The pycnocline thickens considerably during mid-ebb, and the lower layer of stagnant, higher salinity water collapses so that the pycnocline intersects with the bottom.

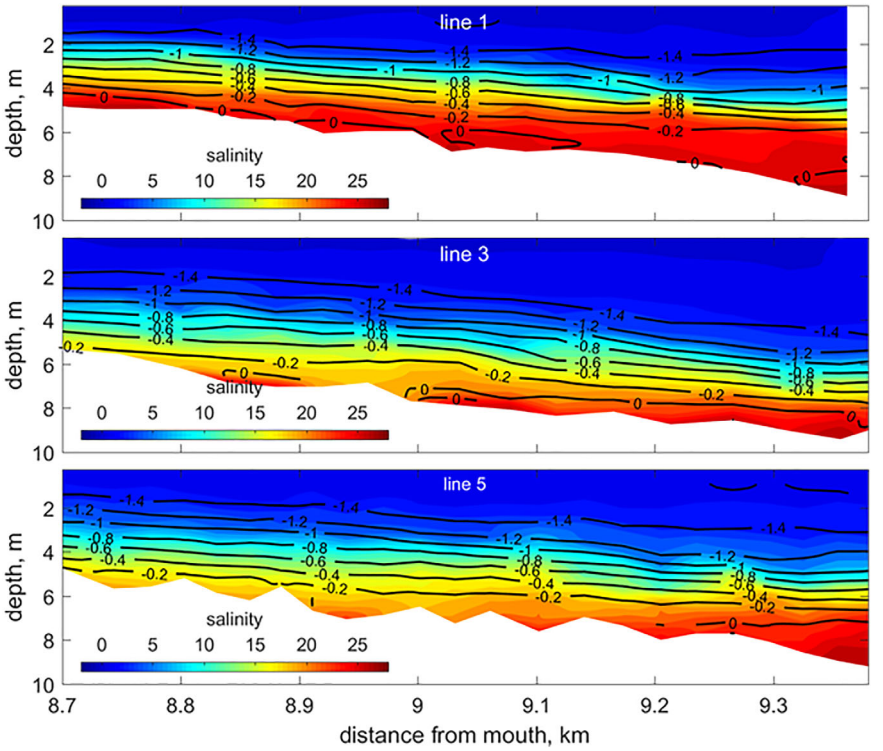

Figure 2. Cross sections of salinity (color contours) and along-channel velocity (line contours) corresponding to Lines 1, 3, and 5, around the time of maximum ebb tide (downestuary is to the left). Velocity and salinity have similar vertical structure, with strong shear and stratification over the 2–3 m thick pycnocline. The pycnocline tilts upward in the seaward direction.

An echo-sounding image obtained during line 5 (Figure 3) shows the familiar braided structure indicative of shear instabilities [*Thorpe*, 1973; *Geyer et al*., 2010; *van Haren and Gostiaux*, 2010]. The braids extend diagonally across the pycnocline, with vertical scales of about 2 m and horizontal spacing of 10–30 m. Smaller-scale features on the braids appear to be secondary instabilities [*Staquet*, 1995]. High intensity backscatter on the braids is likely indicative of high rates of dissipation of salinity variance [*Lavery et al*., 2013]. The irregularity of the bottom echo is an indication of the presence of sand waves (also evident in the high-resolution bathymetry in Figure 1). The position of the instabilities with respect to prominent bed forms suggests that the bed forms may result in perturbations of the flow that contribute to the instabilities, however the velocity resolution was not adequate to address this directly.

Turbulence-resolving measurements from a ship-mounted mast [*Holleman et al*., 2016] provided estimates of turbulent dissipation rate and buoyancy flux and indicated intense mixing in the zone of active shear instabilities. Comparison of those direct measurements of turbulence and mixing with integrated analyses based on Reynolds-averaged profiles is presented in section 4.2.

The salinity measurements could not directly resolve the salinity structure of the braids that was suggested by the acoustic backscatter. However the salinity profiles were used to estimate overturn scales, which were typically on the order of 0.1–0.2 m and rarely more than 0.5 m. This suggests that the overturns were not associated with the primary braid structures but rather with the secondary instabilities within the braids.

Profiles of Ri, based on 0.5 m smoothing of velocity and density profiles to reduce instrument noise and local influence of overturns, are shown for Lines 1, 3, and 5 (Figure 4). The vertical coordinate is salinity (profiles smoothed at 1 m to eliminate overturns) rather than depth in order to emphasize the pycnocline region. In all three lines, the distribution of Ri is close to 0.25 throughout the pycnocline, with median values of 0.26, 0.23, and 0.21 for the three profiles. Later in the ebb when the pycnocline intersects with the bottom, the median value of Ri drops to values of 0.15 or less. This may be due to the influence of the bottom boundary layer on mixing, as shown by *Scully et al*. [2011]. This analysis focuses on the period prior to the intersection of the pycnocline with the bottom, in which the flow acts more like a free shear layer and

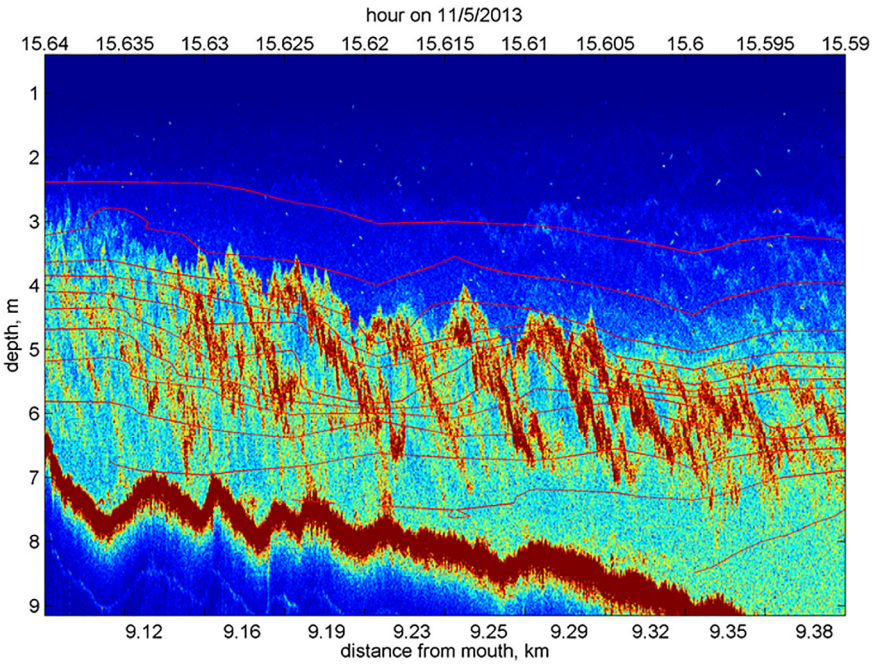

Figure 3. Echo-sounding image (250 kHz) during Line 5,with salinity contours superimposed. Dark blue regions indicate weak backscatter, and dark red is high backscatter. The braid-like structures of shear instabilities are evident in the backscatter throughout the transect. The bottom of the estuary is evident as the thick zone of high backscatter in the lower portion of the figure. The undulations in the bottom elevation are evidence of sand waves (also evident in the high-resolution bathymetry in Figure 1).

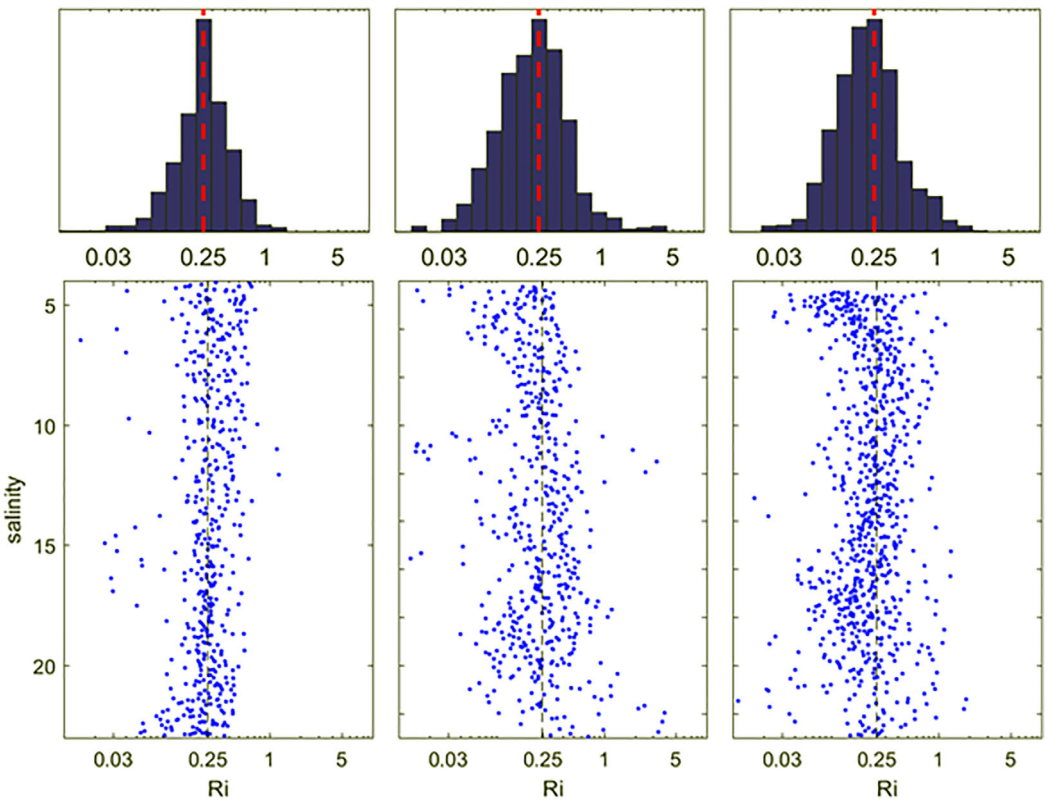

Figure 4. Distributions of Ri for lines 1 (left), 3 (middle), and 5 (right). (top) Histograms of Ri. (bottom) Profiles of Ri versus salinity, so as to emphasize the variation across the pycnocline. The median values of Ri for the three cases were 0.26, 0.23, and 0.21.

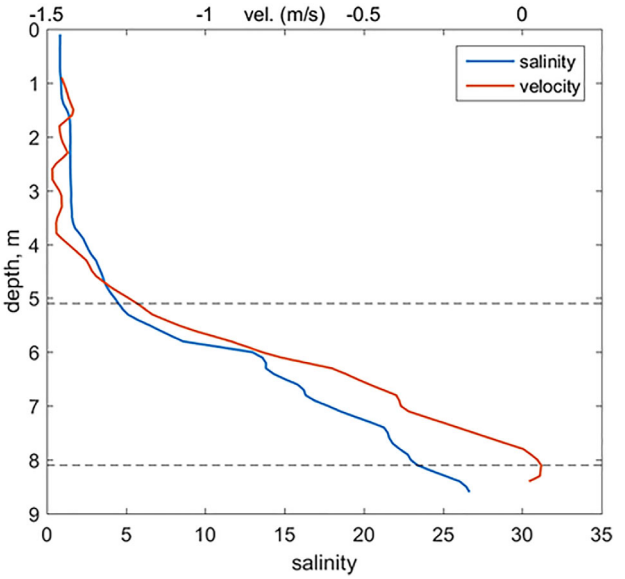

Figure 5. An example of velocity and salinity profiles during line 3, showing the upper (4.5 psu isohaline) and lower (change in shear at top of bottom boundary layer) limits of the pycnocline used to determine Ri_b Note that both velocity and salinity have nearly linear profiles through the pycnocline.

Ri ~ 0.25. To obtain more stable estimates of Ri that were less influenced by local perturbations due to overturns and bathymetry, a bulk estimate Ri_b for the pycnocline was calculated by averaging the shear and stratification over the pycnocline (from the 4.5 psu isohaline to the top of the bottom boundary layer, as determined by a break in slope of the velocity profile—see Figure 5). Estimates of Ri_b for the three selected transects are shown in color in Figure 6, and all of the other transects during mid-ebb conditions are shown in black. These data show that Ri_b tends to remain close to 0.25 through the line during mid-ebb conditions, with 75% of the values falling in the range of 0.2–0.35.

The influence of the scale of vertical averaging of Ri is shown in a comparison of the distributions of Ri and Ri_b (Figure 7). Here Ri is calculated at vertical scales of 0.5 m, whereas Ri_b is averaged over the entire pycnocline (2–3 m). Both Ri and Ri_b are sampled at horizontal spatial scales of about 25 m. The median value of Ri for this sample is 0.21, with 30% of the values falling below 0.15. This indicates that locally unstable conditions occurred almost continuously within this line during maximum ebb flow, consistent with the echo-sounding observations of nearly continuous shear instabilities (Figure 3). While the local Ri was often significantly below 0.25, the value of Ri_b was much closer to 0.25, with a median value of 0.26. The frequent occurrence of $Ri < 0.25$ and $Ri_b \geq 0.25$ suggest that the instabilities were initiated at vertical scales significantly smaller than the 2–3 m scale of the pycnocline. The persistence of $Ri_b \approx 0.25$ suggests that the vertical gradients on average were maintained close to the stability threshold.

A much larger sample of Ri_b was obtained from the moored data located at km 9.05 (in the middle of the line) during month-long observations in October 2015. Because the pycnocline was more coarsely resolved by the seven moored sensors than with the shipboard CTD profile data, a different method was used to estimate Ri_b. The shear and stratification were smoothed at vertical scales of 1.25 m to calculate Ri, and Ri_b was based on the value of smoothed Ri at the middle of the pycnocline (based on the average of surface and bottom salinity). A small amount of data were discarded based on low stratification conditions, as during high run-off periods the salt wedge was flushed downstream from this reach of the estuary.

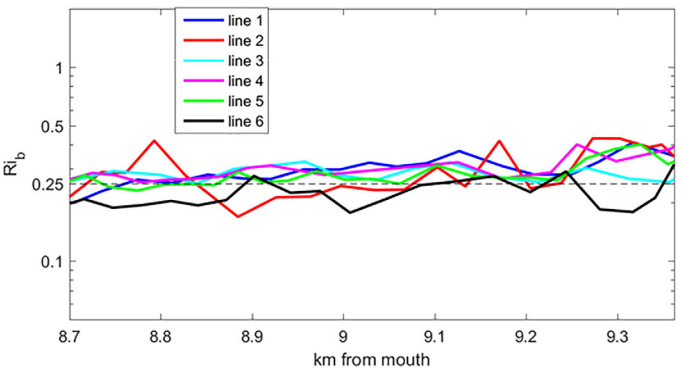

Figure 6. Estimates of Ri_b along the transect in Figure 1 for all of the midebb shipboard observations.

The estimated Ri_b from the month-long time-series was consistently centered on the critical value of 0.25 during midebb (tidal hour 8–10, Figure 8). The median value for Ri_b in the moored time series was 0.26, with 80% of the values between 0.2 and 0.35. These statistics from the moored data were very similar to the shipboard data, again showing the tendency toward an asymptotic behavior of $Ri_b \sim 0.25$. Note that Ri_b has this asymptotic behavior only during

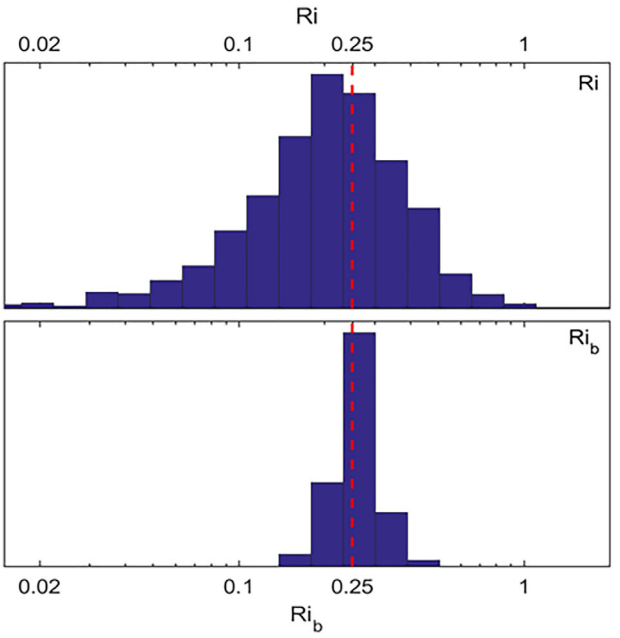

Figure 7. Histograms of Ri and Ri_b for all of the midebb lines. The median value of Ri (0.5 m vertical averaging scale) is 0.21, and the median value of Ri_b (averaged over the pycnocline) is 0.26.

the period of maximum ebb forcing in the region of flow expansion downstream of a topographic constriction.

4. Analysis

The asymptotic behavior of Ri_b provides a constraint on the thickness of the interface, and this in conjunction with the equations for two-layer hydraulics may be used to estimate the mixing rate. Two-layer hydraulics theory is used to estimate the change in interface elevation and shear in response to the changing width of the channel, based on the Froude number at the upstream end of the expanding section. The hydraulic theory is then modified to account for the exchange of momentum and density across the interface in order to satisfy an imposed constraint on the gradient Richardson number. The analysis reveals that for supercritical conditions in an expanding channel, the hydraulic response leads to straining of the interface, decreasing Ri and resulting in mixing. The approach allows an estimate of the rate of mixing, given the upstream Froude number and the geometry of the channel.

4.1. Two-Layer Hydraulics

The hydraulic state of the estuary is based on the composite Froude number G, following *Armi and Farmer* [1986]

$$G^2 = {F_1}^2 + {F_2}^2 = \frac{{u_1}^2}{g' h_1} + \frac{{u_2}^2}{g' h_2} \tag{1}$$

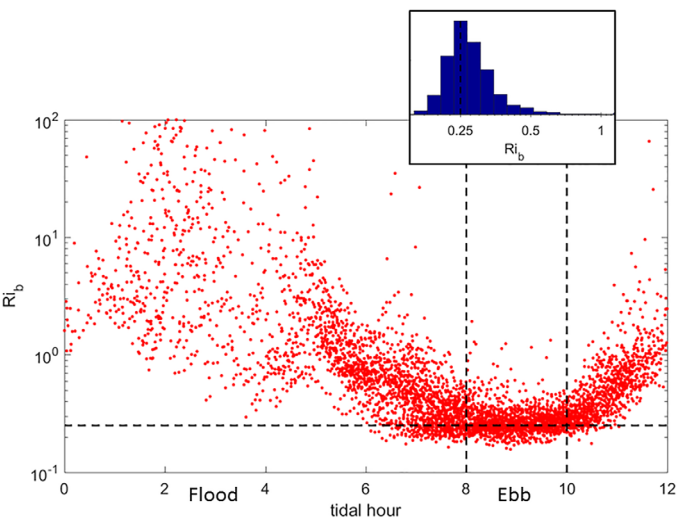

Figure 8. Estimates of Ri_b based on the moored data for a full month in 2015, plotted as a function of tidal phase (hour 0 being the start of flood and hour 6 the start of ebb). The histogram shows the distribution of Ri_b during maximum ebb (hour 8–10), with a median value of 0.26 for this period.

where F_1 and F_2 are layer Froude numbers of the upper and lower layers, u_1 and u_2 are layer-averaged velocities, h_1 and h_2 are the thickness of the upper and lower layer, and $g' = g(\rho_2 - \rho_1)/\overline{\rho}$ is the reduced gravity based on the density difference between the upper and lower layers. The interface between the two layers is locally defined as the elevation at which the salinity is halfway between the water column maximum and minimum salinities. The two-layer approximation is only a rough idealization of the actual velocity and density distribution, due to the continuous variation of shear and stratification through the pycnocline (Figure 2). However the two-layer formulation may be a useful

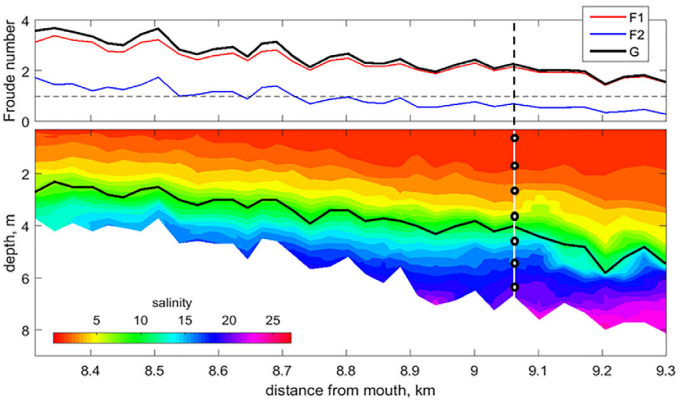

Figure 9. Hydraulic representation of the flow during Line 5. (top) Layer Froude numbers F_1 and F_2 and composite Froude number G, showing increasingly supercritical conditions in the downstream direction (right to left). (bottom) Salinity contours (color) and the estimated interface location dividing the upper and lower layers (black line). The locations of the moored sensors for the 2015 measurements are also shown.

approximation that provides insights that would be obscured in a more complex representation of the flow field.

The estimate of Froude number for the midebb line (Figure 9) shows that the hydraulic state is uniformly supercritical, with a monotonic increase in G from 1.5 to 3.5 in the downstream direction. Note that almost all of the contribution to G comes from F_1, due to the much greater velocities in the upper layer. Froude numbers were also calculated for the large set of moored observations in 2015 (Figure 10). During virtually every ebb tide, $G \approx 2$ at this cross section during maximum ebb, i.e., the hydraulic forcing is consistent and persistent.

The quasi-steady Froude number during the mid-ebb suggests that the steady hydraulics equation may be applicable to explain the essential physics of the regime in this reach of the estuary. For a steady flow in which $F_1 \gg F_2$, the spatial tendency equation for the interfacial elevation can be written as [*Geyer and Ralston*, 2011]

$$\frac{\partial h_i}{\partial x} = \frac{{F_1}^2}{(G^2-1)}\left(\frac{h_1}{W}\frac{\partial W}{\partial x} - C_i\frac{h_o}{h_2}\right) \tag{2}$$

where h_i is the interface elevation relative to a fixed datum, h_o is the total water depth, W is the width of the channel (assumed here to be the width of the upper layer), and C_i is the interfacial drag coefficient, the value of which will be addressed below. This equation indicates that for supercritical conditions, the interface will go up in the downstream direction if the width increases, i.e., if the flow is going through an expansion. This is the same hydraulic regime as a near-field plume at a river mouth [e.g., *MacDonald and Geyer*, 2005]. Interfacial drag always acts in the opposite sense, to reduce the elevation of the interface, however the observations of the monotonically increasing interface elevation indicate that the width effect dominates over the interfacial drag in this setting.

Equation (2) can be used to solve for the along-channel variation of interface elevation by integrating the right hand side in a stepwise manner, starting with upstream values of the Froude numbers and layer thicknesses. The along-channel variation of channel width W provides the "forcing" for each spatial increment, and the velocities are recalculated from mass conservation in each layer, from which the Froude numbers are recalculated. This equation was tested for the conditions during midebb using an idealized approximation for the downstream variation in channel width from 250 to 550 m over approximately 1.2 km (Figure 11). The result for inviscid conditions ($C_i = 0$) is shown as the magenta line in Figure 11. The curvature of the interface elevation reflects the changing contribution of the (G^2 – 1) term in the denominator in (2), which tends to amplify the response when the flow is close to critical.

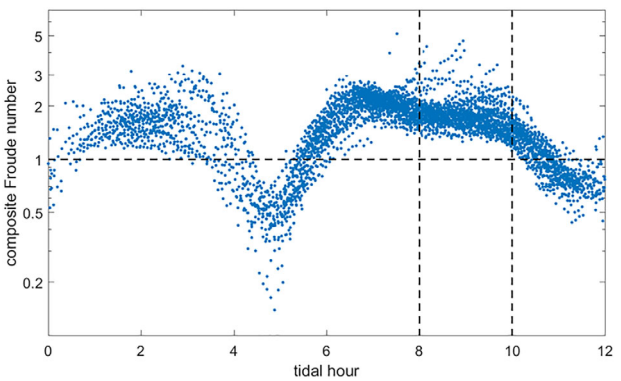

Figure 10. Composite Froude number G based on the moored data from 2015. The flow was always supercritical during the midebb period.

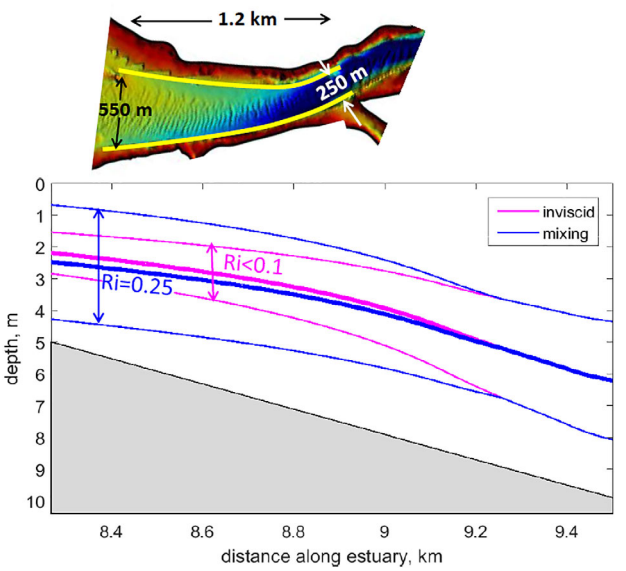

Figure 11. Hydraulic solution for the laterally diverging channel, based on the conditions during Line 5. (top) Map showing the change in width along the line. (bottom) Interface elevation (bold) for the inviscid (magenta) and mixing (blue) cases. The thin magenta lines show the limits of the pycnocline for the inviscid case, and the thin blue lines show the limits of the pycnocline constrained by $Ri_b \geq 0.25$.

The two-layer hydraulic equations do not provide predictions of the interface thickness, but the inviscid variation of interface thickness can be estimated by assuming that the shear and stratification are uniformly distributed across the interfacial layer, which is approximately consistent with the observations (e.g., Figure 5). For the inviscid solution, the interface thins markedly in the downstream direction (Figure 11). This is due primarily to the downstream increase in width, which causes lateral straining of the interfacial layer. There is also a contribution of along-flow straining due to acceleration of the interfacial layer due to the baroclinic pressure gradient. In the inviscid solution, the pressure gradient leads to a significant acceleration along streamlines, leading to longitudinal straining, i.e., $\partial u/\partial x$, within the shear layer.

An important consequence of this lateral and longitudinal straining is that Ri based on the inviscid calculation decreases markedly through the line, starting with a value of Ri = 0.4 in this example and dropping to below 0.1 at the downstream end. This inviscid solution is clearly inconsistent with the observations, both with respect to the observed values of Ri and the observed thickness of the interface. To achieve a viscous solution consistent with the observations, it has been postulated that enough mixing must occur to keep Ri from going below 0.25. This approach has been used as a "turbulence closure" approach by several investigators [e.g., *Price et al*., 1986; *Trowbridge*, 1992]. Vertical mixing within the pycnocline leads to entrainment from above and below, thickening the interface, thereby reducing the shear and increasing the bulk Richardson number Ri_b. With sufficient mixing, Ri_b returns to its threshold value of 0.25.

While the thickening of the interface can readily be determined so as to satisfy the constraint of a critical value of Ri_b, it remains to be determined what the appropriate value of C_i is for a given amount of spreading of the interface. The vertical fluxes of momentum and salt can be calculated based on salt and momentum conservation for a piecewise linear, stratified shear layer. An isopycnal coordinate system provides a frame of reference that is consistent with the two-layer representation of the dynamics—in this reference frame the diapycnal momentum and mass fluxes are due to entrainment, i.e., advection relative to the isopycnal coordinates, and turbulent Reynolds fluxes of momentum and mass. The vertical distributions of entrainment and Reynolds fluxes are derived in Appendix A, based on a specified value of the change in cross-sectional area of the layer due to mixing. The mixing coefficient is defined as

$$\begin{aligned} \overline{u'w'}_{\max} &= C_i(\Delta u)^2 \\ \overline{s'w'}_{\max} &= C_s \Delta u\, \Delta s \end{aligned} \tag{3}$$

where the left hand side of these expressions represent the maximum values of turbulent momentum and salt flux in the water column (slightly above the middle of the pycnocline—see Figures A3 and A4), C_i is the interfacial drag coefficient and C_s is the salt mixing coefficient. The turbulent Prandtl number is assumed to be unity, which means that, consistent with observations, the salinity and velocity gradients are mixed equally.

The results of the analysis from Appendix A indicate that the mixing coefficient can be related to the spreading of the layer via the relation

$$C_i = \alpha \frac{1}{W}\frac{\partial A}{\partial x} \tag{4}$$

where W is the width, A is the cross-sectional area of the pycnocline, and $\alpha \cong 0.064$ is a constant of integration. We also find for the assumption of similar velocity and salinity profiles that $C_s = C_i$. In application to the hydraulic model, the change in cross-sectional area at any location is proportional to the difference between the inviscid thickness of the interface δ_{inv} and the thickness for which Ri = 0.25, or δ_{mix}. Equation (4) then becomes

$$C_i = \alpha \frac{\partial}{\partial x}(\delta_{mix} - \delta_{inv}) \tag{5}$$

where the effects of the changing width and longitudinal acceleration are represented by changes in δ_{inv}. The value of C_i is set to zero for Ri $\geq$ 0.25, for which the interface thickness $\delta = \delta_{inv}$. For Ri $<$ 0.25, the value of C_i is estimated step-wise in a finite-difference calculation moving downstream along the supercritical flow. First the inviscid value is calculated based on equation (2), with C_i set to zero, and if Ri $<$ 0.25, then δ_{mix} is calculated. These quantities are fed into equation (5) to obtain the local value of C_i, and equation (2) is recalculated with that value.

The value of C_i was found to vary between 0.5×10^{-4} and 2×10^{-4} in the regions where mixing occurs, which leads to a significant but not dominant contribution of interfacial mixing to the momentum balance. These are similar values to ones that have been found in estuaries and river plumes [*MacDonald and Geyer*, 2004; *Krvavica et al.*, 2016]. The scaling for the value of the entrainment rate will be discussed below. The important finding of this hydraulic calculation is that the inviscid solution would have a value of Ri much less than 0.25 if there were no mixing, and correspondingly the interface would be much thinner in the absence of mixing than the observations, for which Ri $\approx$ 0.25 and the interface maintains a thickness of several m through the line.

Comparison of the observations with the model-derived pycnocline structure (Figure 12) indicates that the frictional hydraulic model only has a minor influence on the interface elevation, but the frictional solution is consistent with the observations. The significant finding is that the interface is substantially thicker than the inviscid solution, as required by the specification of a critical Richardson number. The details of the structure deviate in certain locations, particularly at the upstream end of the line. This is partly due to the topographical complexity of that part of the estuary, and that the salinity variation in the lower layer cannot be represented by a simple layer model.

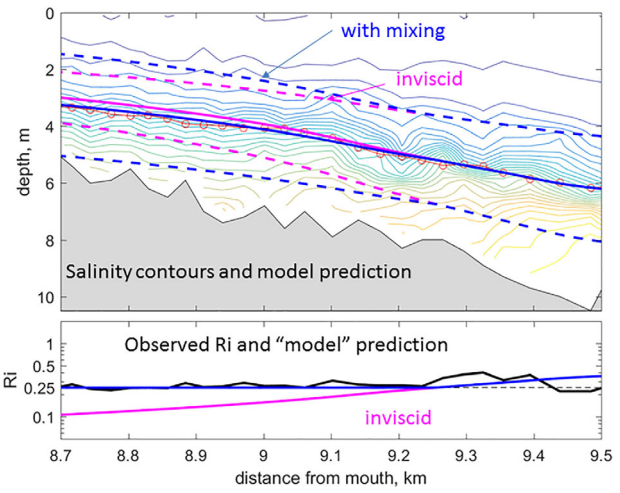

Figure 12. Comparison of the hydraulic solution with the observations for Line 5. (top) Salinity contours with the inviscid (pink) and mixing (blue) solutions superimposed. The red circles indicate the estimated interface location from the data. (bottom) Estimated Ri_b compared with inviscid (pink) and mixing (blue) solutions.

4.2. Quantification of Mixing

An additional test of the validity of this simplified analytical framework is to compare the magnitude of mixing predicted by equation (3) with field observations of mixing. Estimates of turbulent dissipation rate were calculated from the inertial subrange of the vertical velocity at multiple levels in the pycnocline, as reported by *Holleman et al.* [2016]. In the two-layer hydraulic analysis, an estimate of the dissipation rate ε is obtained first by noting that the turbulence production in the pycnocline can be estimated as

$$P = \overline{u'w'}\frac{\partial u}{\partial z} = C_i \frac{{u_1}^3}{\delta} \tag{6}$$

and that $\varepsilon = (1 - Rf)P = 0.78P$, based on $Rf \approx 0.22$ from Holleman et al. For the conditions in Figure 12, the average value calculated for P was 2.1×10^{-4} $m^2 s^{-3}$,

corresponding to $\varepsilon = 1.6 \times 10^{-4}$ m^{2}s^{-3}. For the same line, the average local maximum dissipation was found to be 1.5×10^{-4} m^{2}s^{-3} by Holleman et al. Although this comparison should not be considered as proof of the accuracy of the hydraulics approach for estimating dissipation rate, it provides support for the conceptual model that the mixing is driven by the adjustment of the flow to a critical gradient Richardson number. One significant source of uncertainty in this approach to calculating mixing is the estimation of the lateral spreading rate. The topography may or may not provide a reliable estimate of the lateral divergence of the shear layer, due to flow separation and/or irregularities in channel geometry. Given this uncertainty, the mixing estimates assuming two-layer hydraulics and an equilibrium Ri are probably valid to within a factor of 2, but this is not far from the state of the art in direct measurements of turbulent dissipation and mixing rates in stratified environments.

4.3. A Simplified Expression for the Mixing Coefficient in A Supercritical Expansion

One of the important implications of this work is that the magnitude of the interfacial mixing can be estimated by the hydraulics based on the constraint of the critical Richardson number, without any a priori assumptions about mixing coefficients. Starting with equation (4) and noting that the interface thickness δ remains nearly constant through the mixing zone such that most of the variation in A is due to the increase in width, the average value of C_i in the mixing zone can be approximated by

$$C_i = \alpha \frac{\Delta W}{\overline{W}} \frac{\delta}{L} \tag{7}$$

where ΔW is the change in width over the length of the mixing zone, $\overline{W}$ is the average width, and L is the length of the mixing zone. This expression indicates that the strength of the mixing coefficient depends mainly on the nondimensional amplitude of the geometric forcing and the aspect ratio of the flow, as represented by the ratio of the interface thickness to the horizontal scale of the transition.

Using the geometrical parameters of the mixing zone in the Connecticut River, equation (7) yields an estimate of $C_i \approx 1 \times 10^{-4}$. In order for this scaling to be valid, the flow has to be supercritical (with respect to the composite Froude number), and Ri has to be close to its critical value at the beginning of the mixing zone. The latter constraint is satisfied in supercritical Froude number conditions as long as the initial thickness of the interface is small relative to the water depth. If that constraint is not satisfied, then Ri may remain above its critical value throughout the reach, for example if significant mixing and broadening of the interface had already occurred upstream.

Observations of shear and turbulent dissipation in another location in the Connecticut River (Zone 5 in Figure 1) also produced supercritical conditions, against which this parameterization for mixing could be tested. The estimates of dissipation had much more scatter than the measurements presented above, possibly due to lateral variability of the flow or intermittency. Six estimates were obtained for εranging from 0.2 to 1×10^{-4} m^{2}s^{-3}, with a mean of 5.6×10^{-5} m^{2}s^{-3}. The geometry of this expansion yielded a value of $C_i = 1.5 \times 10^{-4}$, based on equation (7). The velocity difference across the pycnocline was close to 1.0 m/s, and the interface thickness was approximately 3 m. Using equation (6), this yields a turbulence production rate of 5×10^{-5} m^{2}s^{-3}, and a dissipation rate of about 4×10^{-5} m^{2}s^{-3}. This estimate is consistent with the dissipation measurements, albeit without being very tightly constrained due to the scatter in the turbulence measurements.

5. Discussion

5.1. Consideration of Other Hydraulic Forcing Conditions

This analysis demonstrates that mixing is intensified in supercritical flows in divergent estuarine channels, but it does not address other geometries such as a convergent channel or a sill. The divergent channel was found to be particularly conducive to mixing, due to the amplified shear and the thinning of the upper layer. A straight channel would have no hydraulic response (in the absence of bathymetric variations), and a convergent channel would actually cause a thickening of the interface and an increase in Ri. The theory presented here would indicate that no mixing would occur in these conditions, although it would be more accurate to say that mixing would not occur as a result of hydraulic response of the flow. Some mixing would still be expected due to boundary-layer forcing, internal waves, and other perturbations of the shear flow that lead to intermittently subcritical Ri.

This analysis did not include bathymetric forcing of the hydraulic regime, such as the flow over a sill [*Farmer and Armi*, 1989]. The response to topography requires significant flow in the lower layer [*Geyer and Ralston*, 2011], in which case a supercritical flow descending a sloping bottom will have a similar amplification of shear as the case described in this paper. Indeed that is the regime that *Farmer and Armi* [1999] observe downstream of the Sill in Knight Inlet. The theory presented here could be adapted to the case of forcing by a sloping bottom, with two important caveats. First, bottom-intensified flows such as the case described by Farmer and Armi have a significant contribution of bottom stress to the dynamics and possibly to the mixing. Second, the presence of a hydraulic jump provides another source of mixing that would have to be considered. In any case, the straining of the interface in supercritical flows over topography may be an important and readily quantified source of mixing in estuaries, fjords, and other oceanic environments.

5.2. Application to Partially Mixed Estuaries

Although the two-layer hydraulic theory is generally applied to highly stratified estuaries such as salt wedges and fjords, *Chant and Wilson* [2000] applied hydraulic theory to observations of the Hudson River estuary, in which they noted an amplification of the shear under supercritical flow conditions, consistent with the results of the present study. *Peters and Bokhorst* [2000] made high-resolution measurements of turbulence in the Hudson estuary, noting an enhancement of turbulent dissipation in regions of supercritical hydraulic response. They made measurements during both neap and spring tides, and their neap-tide measurements appear to be more relevant to this study based on the strength of the stratification. They observed a dissipation rate of around 0.5×10^{-5} m^2s^{-3} in the middle of the pycnocline in the region of lateral divergence [*Peters and Bokhorst*, 2000, Figure 5]. Applying the scaling developed from the Connecticut (equation (7)) to the Hudson case, we estimate roughly a 30% increase in width over 3 km for the reach of the Hudson estuary of their measurements and calculate a $C_i = 0.7 \times 10^{-4}$ (with an assumed shear layer thickness $\delta = 10$ m). With an estimated velocity difference of 1 m/s over the shear layer, the estimated production (equation (6)) is 0.7×10^{-5} m^2s^{-3}, roughly consistent with their dissipation estimates. Although this is not a rigorous test of the theory, it suggests that the applicability of the approach may extend to other estuarine regimes.

The results of *Peters and Bokhorst* [2000] for spring-tide conditions in the Hudson estuary provide an example in which the approach of this paper would not be expected to work, because in spring tide conditions the dynamics are no longer well represented by two-layer hydraulics due to the dominance of boundary-generated mixing. During spring tides in the Hudson, there was no longer a distinct separation between upper and lower layers, and the gradient Richardson number was less than 0.1 over most of the water column [*Peters and Bokhorst*, 2000, Figure 5]. The observations in the Connecticut River showed a similar drop in Ri late in the ebb, when boundary layer processes began to dominate, and the two-layer approach was no longer valid [*Holleman et al*., 2016].

5.3. Application to River Plumes

Another relevant application is the nearfield of river plumes, where the buoyant plume spreads laterally as it enters the ocean [*Hetland*, 2010; *Horner-Devine et al*., 2015; *MacDonald and Chen*, 2012]. Near-field river plumes satisfy the two constraints of the theory presented here, the supercritical Froude number conditions and lateral expansion. *MacDonald and Chen* [2012] specifically address the relationship between lateral expansion and mixing in a river plume, based on observations in the Merrimack River plume. They define a nondimensional mixing parameter

$$\xi = \frac{B}{g' u_1} \tag{8}$$

where $B = (g/\rho)\overline{\rho' w'}$ is the mixing-induced vertical buoyancy flux. Based on the assumption that the mixing coefficients are the same for mass and momentum (which is consistent with the observation that the shear layer and pycnocline spread at the same rate), $\xi = C_i$, i.e., MacDonald and Chen's buoyancy mixing parameter is quantitatively equal to the mixing parameter C_i based on vertical momentum flux. MacDonald and Chen indicate that the mixing rate depends on the spreading rate, which they nondimensionalize as

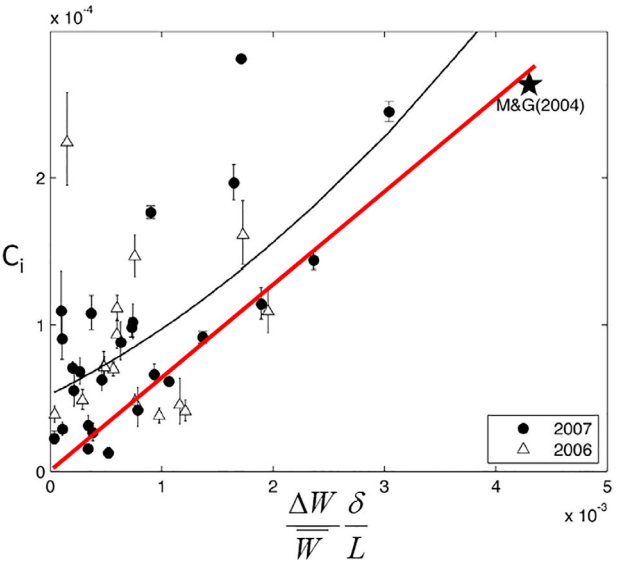

Figure 13. Estimates of interfacial mixing coefficient versus lateral spreading rate for various river plume observations from *MacDonald and Chen* [2012] compared with equation (7) (red line). The black line is the fit suggested by MacDonald and Chen. Note that the slope of the red line is α.

$$\phi = \frac{\Delta W}{\overline{W}} \frac{\delta}{L} \tag{9}$$

where the notation of this paper has been substituted for their notation. According to equation (7), MacDonald and Chen's mixing parameter should depend linearly on ϕ, with a slope of α. A comparison of their results with this relation is shown in Figure 13. The linear relation is consistent with many of their observations (including the results of *MacDonald and Geyer* [2004] from the front at the mouth of the Fraser River, shown as a star). Interestingly about half of their observations collapse onto the linear scaling, and the others show significantly elevated values, with considerable scatter. The elevated values are indicative of greater mixing than predicted by equation (7), possibly indicating other mixing processes unrelated to the spreading rate.

MacDonald and Chen suggest that the dependence of mixing on spreading is due to vortex stretching of shear instabilities that enhances mixing. In essence the mechanism invoked in this paper is similar, albeit without considering the details of the shear instability mechanism. In both cases, the lateral straining of the shear layer is invoked as the forcing mechanism for mixing. In this paper, the constraint of the critical Richardson number is used to quantify the response to that straining, leading to a quantitative scaling estimate for the relationship between straining and mixing.

5.4. Application to Oceanic Overflows

Another relevant comparison is the estimation of entrainment coefficients for overflows, starting with the work of *Ellison and Turner* [1959] and more recently synthesized by *Cenedese and Adduce* [2010]. They considered flows in which the lower layer is the hydraulically active layer, which differs from the present case with respect to the potential role of the bottom boundary layer. However, the interfacial mixing processes would be expected to be similar, particularly at high Fr, so the comparison could be informative. Their entrainment coefficient E is approximately equivalent to C_i, based on the assumption that the mixing coefficients for salt and momentum are the same. Considering a range of scales from large field cases such as the Baltic Sea and Denmark Strait to laboratory experiments, they find entrainment coefficients varying from 10^{-5} to 10^{-1}, with the field cases typically on the order of 10^{-4} and the laboratory cases 1 to 2 orders of magnitude greater. *Cenedese and Adduce* [2010] obtain reasonable collapse of this large spread between field and laboratory data with an inverse dependence on Reynolds number, specifically $\mathrm{Re}^{-1/2}$, such that the mixing rate decreases roughly in proportion to the scale of the flow. Viscous and molecular mixing processes would be expected to be relevant at the low Re of laboratory conditions, but viscous processes do not contribute measurably to momentum exchange in energetic, high-Re oceanic flows, so asymptotic behavior with respect to Re is expected. The results of this investigation suggest that the aspect ratio h_o/L may also be an important consideration, and may explain some of the spread between laboratory and field cases, as laboratory flows typically have aspect ratios 1 to 2 orders of magnitude greater than field cases. Future attempts to parameterize entrainment rates should consider the geometry of the flow, and most notably the potential role of aspect ratio as a controlling variable.

5.5. Comparison With Other Parameterizations of Ri-Dependent Mixing

The approach presented in this paper to quantifying mixing follows *Trowbridge* [1992] in assuming that the amount of mixing is whatever is required to maintain $\mathrm{Ri} = 0.25$. This differs from popular closure formulations that specify a mixing rate that varies as a strong function of Ri below some assigned threshold, e.g.,

the stability functions of *Kantha and Clayson* [1994], which are very effective for model representations of stratified shear flows [*Umlauf and Burchard*, 2005], or the Ri-dependent closure of *Kunze et al*. [1990], which has been applied successfully to oceanic mixing [e.g., *Polzin*, 1996] and to mixing in a river plume [*Jurisa et al*., 2016]. In practice these approaches are not substantially different from the approach used in this paper, because of the strong sensitivity of the mixing rate to Ri as it decreases below its critical value. Using the *Kunze et al*. [1990] case as an example, an order of magnitude increase in mixing occurs between Ri = 0.24 and 0.22. That small difference in Ri would be difficult to resolve with measurements (cf., Figure 7), yet it represents a vast difference in the strength of mixing. The results of this study are not inconsistent with the Ri-dependent closure approaches, but the hydraulics provide a stronger constraint on the mixing rate in context with measurable quantities in field observations.

6. Summary and Conclusions

These observations provide strong evidence that the threshold of mixing of a stratified shear flow corresponds to the theoretical value of Ri = 0.25. While instantaneous values of Ri have considerable scatter around that threshold value, averages over the pycnocline in regions of active mixing tend to converge toward a value of 0.25. An important caveat is that for mixing to occur, the topographic forcing must be strong enough to drive Ri below 0.25. In this case, the forcing was due to lateral bathymetric expansion in the downstream flow direction, leading to straining of the shear layer by lateral spreading of the supercritical flow. The two-layer hydraulic equations provide a framework for quantifying the strain rate, and the constraint that Ri = 0.25 then provides a means of quantifying the mixing rate within the pycnocline. The result of this analysis indicates that the mixing coefficient depends linearly on the product of the topographic forcing and the aspect ratio of the flow. This scaling is similar to that obtained by *MacDonald and Chen* [2012] for mixing in river plumes, but in this case the scaling factor is determined analytically, based on the relationship between the vertical spreading rate of the layer and the mixing rate. This analysis suggests that the mixing coefficient for other supercritical flow regimes, such as oceanic overflows, may also have aspect-ratio dependence, which may explain in part the large differences between mixing rates in laboratory and large-scale, oceanic flow regimes.

Appendix A: Entrainment and Mixing in A Stratified Shear Layer

The approximation of linear velocity and salinity profiles through the pycnocline allows an analytic calculation of the vertical distribution of entrainment and turbulent momentum and salt fluxes, based on the constraints that the flow is steady and that salt is conserved. The configuration is shown in Figure Figure A1, where the vertical coordinate system has an origin at the base of the pycnocline of thickness δ, so the position within the pycnocline is represented by z/δ, the lower layer salinity is s_0 and the upper layer is completely fresh, and the salinity and velocity are represented by

$$s = s_o\left(1-\frac{z}{\delta}\right) \tag{A1}$$

$$u = u_o\frac{z}{\delta} \tag{A2}$$

The width W and pycnocline thickness δ both vary in the downstream direction, their product being the area $A = \delta W$, which increases as $\partial A/\partial x$ due to increases in width and pycnocline thickness. If u_o remains constant, then the increase in A in the downstream direction requires that the transport increase, which requires entrainment from above and/or below the interface. The total entrainment can be estimated by

$$\left(w_{e,bot}-w_{e,top}\right)W = \frac{\partial Q}{\partial x} = \frac{\partial}{\partial x}\int_0^\delta uWdz = \frac{1}{2}u_o\frac{\partial A}{\partial x} \tag{A3}$$

where $w_{e,bot}$ is the entrainment velocity at the bottom of the pycnocline (upward positive) and $w_{e,top}$ is entrainment at the top, which will be seen to be negative, i.e., into the layer. Although this equation does not specify the relative contributions of upward and downward entrainment, the divergence of salt flux can

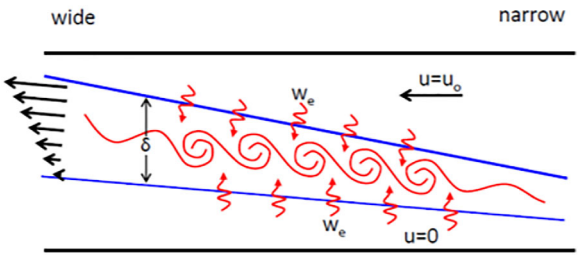

Figure A1. Configuration of the domain, showing a stratified shear flow with a pycnocline of thickness δ that thickens and widens laterally in the downstream direction. Entrainment from above and below balance the divergence of transport in the shear layer.

only be satisfied by entrainment from below, as the salinity is zero at the top of the layer. The magnitude of entrainment is determined by considering the vertically integrated salt flux divergence equation

$$s_o w_{e,bot} W = \frac{\partial Q_S}{\partial x} = \frac{\partial}{\partial x}\int_0^\delta suWdz = \frac{1}{6} s_o u_o \frac{\partial A}{\partial x} \tag{A4}$$

where Q_S is the volumetric salt transport. Having specified its value at the bottom, an expression for the vertical structure of the entrainment coefficient is obtained by integrating the continuity equation

$$w_e = w_{e,bot} + \frac{1}{W}\frac{\partial}{\partial x}\int_0^z uWdz' = \frac{1}{W} u_o \frac{\partial A}{\partial x}\left(\frac{1}{6} - \frac{1}{2}\frac{z^2}{\delta^2}\right) \tag{A5}$$

The vertical structure of w_e (Figure Figure A2) shows that entrainment is convergent in the vertical direction, with downward entrainment in the upper part of the pycnocline and upward entrainment in the lower portion. The asymmetry of entrainment is due to the shear, which leads to stronger divergence in the upper part of the pycnocline.

Entrainment across salinity surfaces can only happen in combination with mixing—in fact it can only happen if the rate of mixing varies in the cross-isopycnal direction. This can be shown by considering the one-dimensional (vertical) conservation equation for salinity

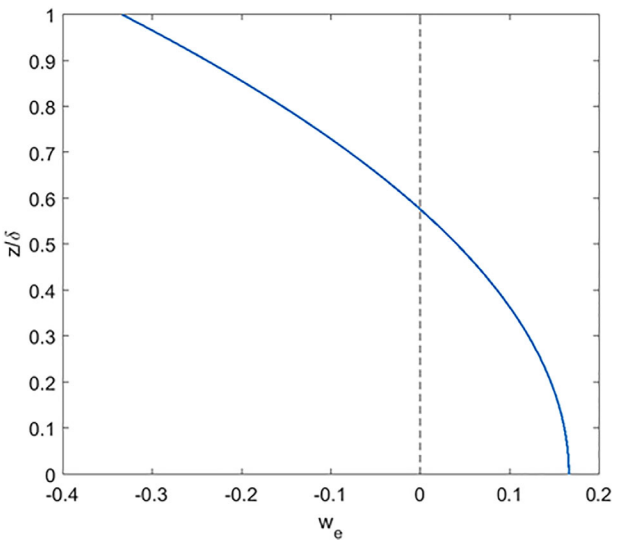

Figure A2. Entrainment velocity w_e (equation (A5)) (scaled by $(u_o/W)\partial A/\partial x$) as a function of nondimensional position in the pycnocline.

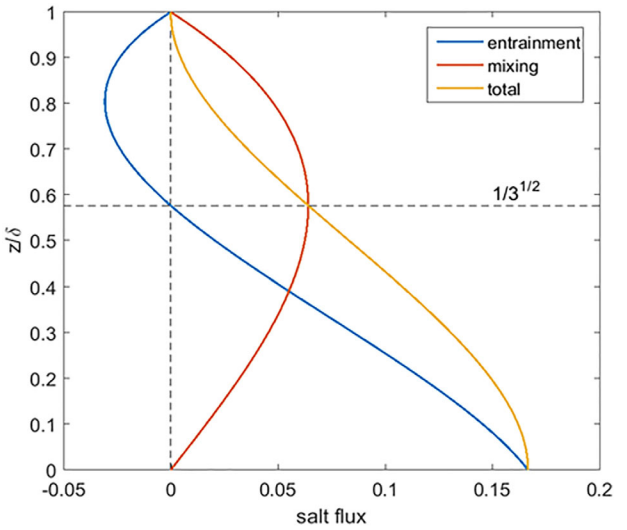

Figure A3. Salt flux due to entrainment $w_e s(z)$ (equations (A1) and (A5)) (blue), turbulent salt flux $s'w'$ (equation (A9)) (red), and the total (yellow). The maximum mixing occurs where entrainment goes to zero, at a relative height of $1/3^{1/2}$.

$$\frac{\partial s}{\partial t} + w\frac{\partial s}{\partial z} = -\frac{\partial}{\partial z}\overline{s'w'} \tag{A6}$$

where s and w are Reynolds-averaged salinity and vertical velocity and $\overline{s'w'}$ is the vertical turbulent salt flux. Transforming to isohaline coordinates so that the reference frame moves vertically with the Reynolds-averaged salinity eliminates the time-dependent term, and w becomes w_e, the velocity relative to the isohaline, or the entrainment velocity. The vertical mixing is the same, because the change in reference frame does not alter the correlations of the fluctuations. The vertical coordinate is replaced by the salinity coordinate via

$$\frac{\partial}{\partial z} = \frac{\partial s}{\partial z}\frac{\partial}{\partial s} \tag{A7}$$

As long as $\partial s/\partial z$ does not vanish, the transformed equation becomes simply

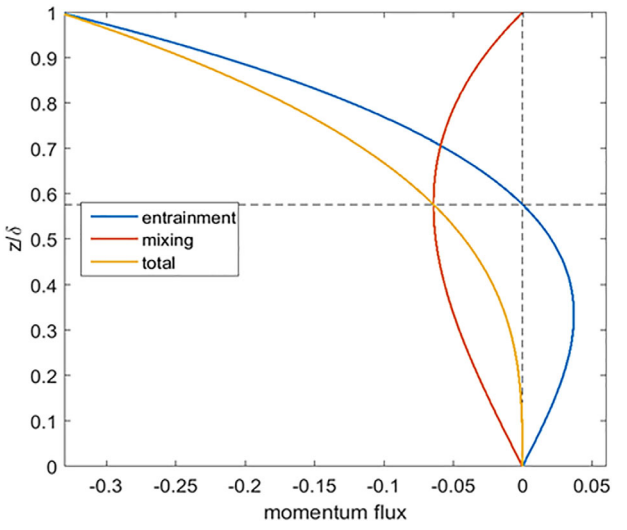

Figure A4. Momentum flux due to entrainment $w_e\, u(z)$ (equations (A2) and (A5)) (blue), turbulent momentum flux u'w' (equation (A10)) (red), and the total (yellow). The magnitude of the nondimensional salt flux and momentum flux at the point of maximum mixing (zero entrainment) is equal to $\alpha \sim 0.064$.

$$w_e = -\frac{\partial}{\partial s}\overline{s'w'} \tag{A8}$$

which was also demonstrated by *McDougall and Dewar* [1998]. Note that entrainment can go either direction with respect to the salinity gradient, but it always goes in the direction of greater mixing, as will be evident in this example.

This expression can be integrated to obtain the rate of turbulent salt flux based on the vertical distribution of w_e.

$$\overline{s'w'} = \int_0^s w_e ds = \int_0^z w_e \frac{\partial s}{\partial z} dz' = \frac{1}{W} u_o s_o \frac{\partial A}{\partial x} \frac{1}{6} \frac{z}{\delta} \left(1 - \frac{z^2}{\delta^2}\right) \tag{A9}$$

The vertical distribution of $\overline{s'w'}$ has a nearly parabolic shape (Figure Figure A3), going to zero at the top and bottom of the pycnocline and reaching a maximum at $z/\delta = 1/\sqrt{3}$, which is where $w_e = 0$, consistent with equation (A8). Note that while mixing is everywhere downgradient, the salt flux due to entrainment is countergradient in the upper part of the water column. The total salt flux (sum of mixing and entrainment) is everywhere downgradient and monotonically decreasing in the vertical. The convergence of this vertical flux exactly balances the divergence of horizontal flux due to the increasing cross section of the pycnocline in the downstream direction.

A similar analysis can be performed for the velocity structure, with essentially the same result as for salt (Figure A4).

$$\overline{u'w'} = -\frac{1}{W} {u_o}^2 \frac{\partial A}{\partial x} \frac{1}{6} \frac{z}{\delta} \left(1 - \frac{z^2}{\delta^2}\right) \tag{A10}$$

However because the sign of the shear is the opposite of the salinity gradient, mixing of momentum is everywhere downward. The flux of momentum by entrainment changes sign in the middle of the water column, just as for salinity. The total vertical momentum flux is everywhere negative (high momentum fluid being transported downward), and the vertical convergence of momentum flux linearly decreases through the shear layer, consistent with the vertical variation of divergence of horizontal momentum flux.

A value of the interfacial drag coefficient is determined by the relationship

$$C_i |\Delta u| \Delta u = \overline{u'w'} \tag{A11}$$

at some representative mid-pycnocline location. The location of the maximum in $\overline{u'w'}$ is also the location where all of the momentum flux is conveyed by mixing (as opposed to entrainment), so it appears to be the appropriate level to define the interfacial drag coefficient. Its value based on A10 evaluated at $z/\delta = 1/\sqrt{3}$ is

$$C_i = \alpha \frac{1}{W} \frac{\partial A}{\partial x} \tag{A12}$$

where $\alpha = 1/9\sqrt{3} \approx 0.064$. Now we note that if u_o is constant, as was assumed for this simplified analysis, then for the inviscid case the area of the pycnocline would remain constant in order to conserve volume flux in the layer. However in the case with shear-induced mixing, the area of the pycnocline increases exactly in proportion to its increasing thickness due to mixing. Its width stays the same, and so we find that

$$\frac{1}{W} \frac{\partial A}{\partial x} = \frac{\partial}{\partial x} (\delta_{mix} - \delta_{inv}) \tag{A13}$$

and so

$$C_i = \frac{1}{9\sqrt{3}} \frac{\partial}{\partial x} (\delta_{mix} - \delta_{inv}) \cong 0.064 \frac{\partial}{\partial x} (\delta_{mix} - \delta_{inv}) \tag{A14}$$

Acknowledgments
The authors would like to recognize Jay Sisson for his management of the field operations on the Connecticut River. All the data used in this paper can be obtained by request of the first author at rgeyer@whoi.edu. The field study and the coauthors' contributions were supported by NSF grant OCE 0926427. Holleman was also supported by the Devonshire Scholars program.

References

Armi, L., and D. Farmer (1986), Maximal two-layer exchange flow through a contraction with barotropic net flow, *J. Fluid Mech.*, *164*, 27–51.
Balsley, B. B., G. Svensson, and M. Tjernström (2008), On the scale-dependence of the gradient Richardson number in the residual layer, *Boundary Layer Meteorol.*, *127*, 57–72.
Cenedese, C., and C. Adduce (2010), A new parameterization for entrainment in overflows. *J. Phys. Oceanogr.*, *40*, 1835–1850.
Chant, R. J., and R. E. Wilson (2000), Internal hydraulics and mixing in a highly stratified estuary, *J. Geophys. Res.*, *105*, 14,215–14,222.
Ellison, T. H., and J. S. Turner (1959), Turbulent entrainment in stratified flows, *J. Fluid Mech.*, *6*, 423–448.
Farmer, D. F., and L. Armi (1999), Stratified flow over topography: The role of small scale entrainment and mixing in flow establishment, *Proc. R. Soc. London, Ser. A*, *455*, 3221–3258.
Farmer, D. F., and J. D. Smith (1980), Tidal interaction of stratified flow with a sill in Knight Inlet, *Deep Sea Res., Part A*, *27*, 239–254.
Geyer, W. R., and D. M. Farmer (1989), Tide induced variation of the dynamics of a salt wedge estuary, *J. Phys. Oceanogr.*, *28*, 1060–1072.
Geyer, W. R., and D. K. Ralston (2011), The dynamics of strongly stratified estuaries, in *Treatise on Estuarine and Coastal Science*, edited by E. Wolanski and D. S. McLusky, vol. 2, pp. 37–51, Academic, Waltham, Mass.
Geyer, W. R., and J. D. Smith (1987), Shear instability in a highly stratified estuary, *J. Phys. Oceanogr.*, *17*, 1668–1679.
Geyer, W. R., A. C. Lavery, M. E. Scully, and J. H. Trowbridge (2010), Mixing by shear instability at high Reynolds number, *Geophys. Res. Lett.*, *37*, L22607, doi:10.1029/2010GL045272.
Hazel, P. (1972), Numerical studies of the stability of inviscid stratified shear flows, *J. Fluid Mech.*, *51*, 39–61.
Hetland, R. D. (2010), The effects of mixing and spreading on density in near-field river plumes, *Dyn. Atmos. Oceans*, *49*, 37–53.
Holleman, R. C., W. R. Geyer, and D. K. Ralston (2016), Stratified turbulence and mixing efficiency in a salt wedge estuary, *J. Phys. Oceanogr.*, *46*, 1769–1783.
Horner-Devine, A. R., R. D. Hetland, and D. G. MacDonald (2015), Mixing and transport in coastal river plumes, *Annu. Rev. Fluid Mech.*, *47*, 569–594.
Jurisa, J. T., J. D. Nash, J. N. Moum, and L. F. Kilcher (2016), Controls on turbulent mixing in a strongly stratified and sheared tidal river plume, *J. Phys. Oceanogr.*, *46*, 2373–2388.
Kantha, L. H., and C. A. Clayson (1994), An improved mixed layer model for geophysical applications, *J. Geophys. Res.*, *99*, 25,235–25,266.
Krvavica, N., V. Travas, and N. Ozanic (2016), A field study of interfacial friction and entrainment in a microtidal salt-wedge estuary, *Environ. Fluid Mech.*, *16*, 1223–1246, doi:10.1007/s10652-016-9480-1.
Kunze, E, A. J. Williams, and M. G. Briscoe (1990), Observations of shear and vertical stability from a neutrally buoyant float, *J. Geophys. Res.*, *95*, 18,127–18,142.
Lavery, A. C., W. R. Geyer, and M. E. Scully (2013), Broadband acoustic imaging and quantification of stratified turbulence, *J. Acoust. Soc. Am.*, *134*, 40–54.
MacDonald, D. G., and F. Chen (2012), Enhancement of turbulence through lateral spreading in a stratified-shear flow: Development and assessment of a conceptual model, *J. Geophys. Res.*, *117*, C05025, doi:10.1029/2011JC007484.
MacDonald, D. G., and W. R. Geyer (2004), Turbulent energy production and entrainment at a highly stratified esturarine front, *J. Geophys. Res.*, *109*, C05004, doi:10.1029/2003JC002094.
MacDonald, D. G., and W. R. Geyer (2005), Hydraulic control of a highly stratified estuarine front, *J. Phys. Oceanogr.*, *35*, 374–386.
MacDonald, D. G., and A. R. Horner-Devine (2008), Temporal and spatial variability of vertical salt flux in a highly stratified estuary, *J. Geophys. Res.*, *113*, C09022, doi:10.1029/2007JC004620.
McDougall, T. J., and W. K. Dewar (1998), Vertical mixing and cabbeling in layered models, *J. Phys. Oceanogr.*, *28*, 1458–1480.
Miles, J. W. (1961), On the stability of heterogeneous shear flows, *J. Fluid Mech.*, *10*, 496–508.
Partch, E. N., and J. D. Smith (1978), Time dependent mixing in a salt wedge estuary, *Estuarine Costal Mar. Sci.*, *6*, 3–19.
Peters, H. (2003), Broadly distributed and locally enhanced turbulent mixing in a tidal estuary, *J. Phys. Oceanogr.*, *33*, 1967–1977.
Peters, H., and R. Bokhorst (2000), Microstructure observations of turbulent mixing in a partially mixed estuary: Part I: Dissipation rate, *J. Phys. Oceanogr.*, *30*, 1232–1244.
Peters, H., M. C. Gregg, and J. M. Toole (1988), On the parameterization of equatorial turbulence, *J. Geophys. Res.*, *93*, 1199–1218.
Polzin, K. (1996), Statistics of the Richardson number: Mixing models and fine structure, *J. Phys. Oceangr.*, *26*, 1409–1425.
Price, J. F., R. A. Weller, and R. Pinkel (1986), Diurnal cycling: Observations and models of the upper ocean response to diurnal heating, cooling and wind mixing, *J. Geophys. Res.*, *91*, 8411–8427.
Ralston, D. A., W. Rockwell Geyer, and J. A. Lerczak (2010), Structure, variability and salt flux in a strongly forced estuary, *J. Geophysical Res.*, *115*, C06005, doi:10.1029/2009JC005806.
Schijf, J. B., and J. C. Schonfeld (1953), Theoretical considerations on the motion of salt and fresh water, in *Proceedings of the Minnesota International Hydraulics Convention, 5th Congress IAHR*, pp. 321–333, University of Minnesota, Univ. Minnesota Press, Minn.
Scully, M. E., W. Rockwell Geyer, and J. H. Trowbridge (2011), The influence of stratification and non-local turbulent production on estuarine turbulence: An assessment of turbulence closure with field observations, *J. Phys. Oceanogr.*, *41*, 166–185.
Staquet, C. (1995), Two-dimensional secondary instabilities in a strongly stratified shear layer, *J. Fluid Mech.*, *296*, 73–126.
Thorpe, S. A. (1973), Experiments on instability and turbulence in a stratified shear flow, *J. Fluid Mech.*, *61*, 731–751.
Trowbridge, J. H. (1992), A simple description of the deepening and structure of a stably stratified flow driven by a surface stress, *J. Geophys. Res.*, *97*, 15,529–15,543.
Umlauf, L., and H. Burchard (2005), Second-order turbulence closure models for geophysical boundary layers: A review of recent work, *Cont. Shelf Res.*, *25*, 795–827.
Van Haren, H., and L. Gostiaux (2010), A deep-ocean Kelvin-Helmholtz billow train, *Geophys. Res. Lett.*, *37*, L03605, doi:10.1029/2009GL041890.